

Supplementary Material

Spin crossover and reversible single-crystal to single-crystal transformation behaviour in two cyanide-bridged mixed-valence $\{\text{Fe}^{\text{III}}_2\text{Fe}^{\text{II}}_2\}$ clusters

Chunyang Zheng,^{a,b,†} Juping Xu,^{a,‡} Feng Wang^c, Jun Tao^d and Dongfeng Li*^{a,d}

^a College of Chemistry, Key Laboratory of Pesticide and Chemical Biology of Ministry of Education, Central China Normal University, 430079 Wuhan

^b Hubei Collaborative Innovation Center for Rare Metal Chemistry, Hubei Key Laboratory of Pollutant Analysis and Reuse Technology, Institute for Advanced Materials, Hubei Normal University, 435002 Huangshi, P. R. China

^c College of Chemistry and Materials Science, Hubei Engineering University, 432000 Xiaogan, P. R. China.

^d State Key Laboratory of Physical Chemistry of Solid Surfaces, Xiamen University, 361005 Xiamen, P. R. China

† These authors contributed equally to this work.

*E-mail: dfli@mail.ccnu.edu.cn

CONTENTS

Figure S1 FT-IR for 1	S3
Figure S2 Cyclic voltammograms of complex 1 in MeCN.....	S3
Figure S3 ESI-MS spectrum for 2·H₂O	S4
Figure S4 ESI-MS spectrum for 3·MeOH	S4
Figure S5 X-ray powder diffraction diagrams of 2·H₂O	S5
Figure S6 X-ray powder diffraction diagrams of 3·MeOH	S5
Figure S7 Variable-temperature FT-IR for 2·H₂O	S6
Figure S8 Variable-temperature FT-IR for 3·MeOH	S6
Figure S9 Thermo-gravimetric analysis of 2·H₂O	S7
Figure S10 Thermo-gravimetric analysis of 3·MeOH	S7
Figure S11 Thermo-gravimetric analysis of 3·2H₂O	S8
Figure S12 Temperature dependence of $\chi_M T$ plots for 3·MeOH and 3·2H₂O	S8
Figure S13 Temperature dependence of $\chi_M T$ plot for 1	S9
Figure S14 Schematic representation between 2·H₂O and 2	S9
Figure S15 Schematic representation between 3·MeOH and 3·2H₂O	S9
Figure S16 Dihedral angle about SCO Fe site in 2	S10
Figure S17 Dihedral angle about SCO Fe site in 3	S10
Figure S18 Dihedral angles in $[\text{Fe}^{II}_4(\text{CN})_4(\text{bpy})_4(\text{tpa})_4](\text{PF}_6)_4$	S11
Table S1 Crystal data and structure refinement for 1	S12
Table S2 Selected bond lengths and angles for 1	S13

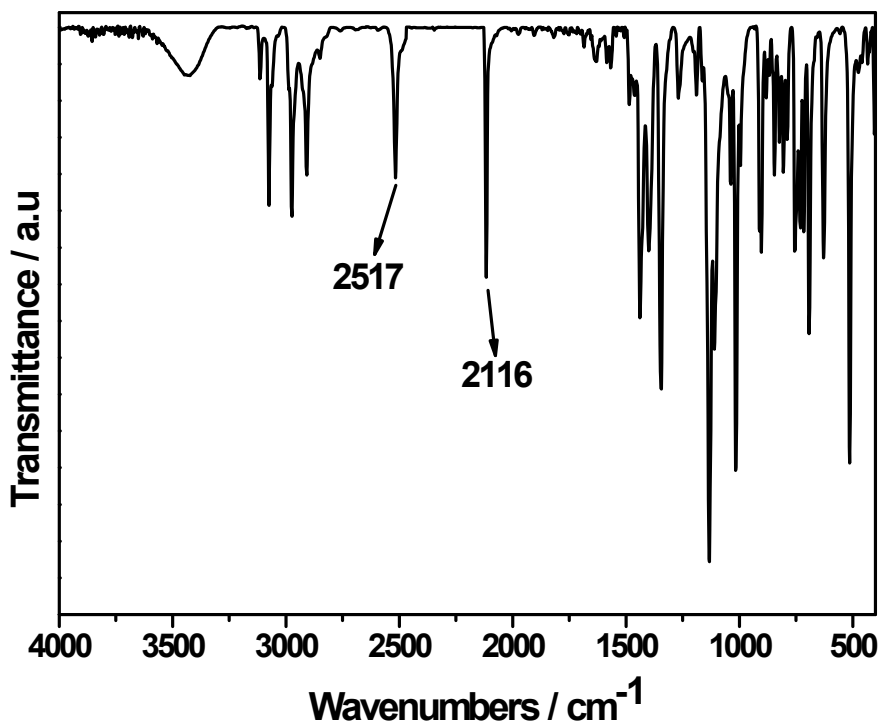


Figure S1 FT-IR for **1** at room temperature.

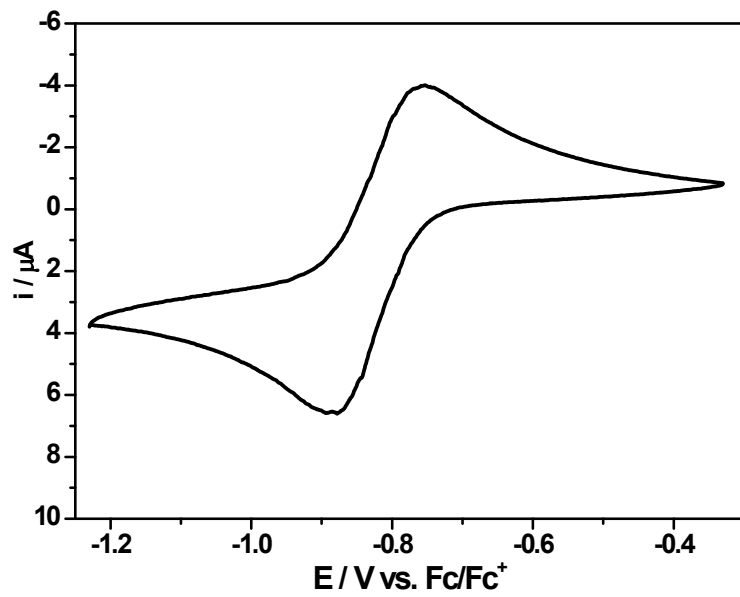


Figure S2 Cyclic voltammogram of complex **1** in CH₃CN.

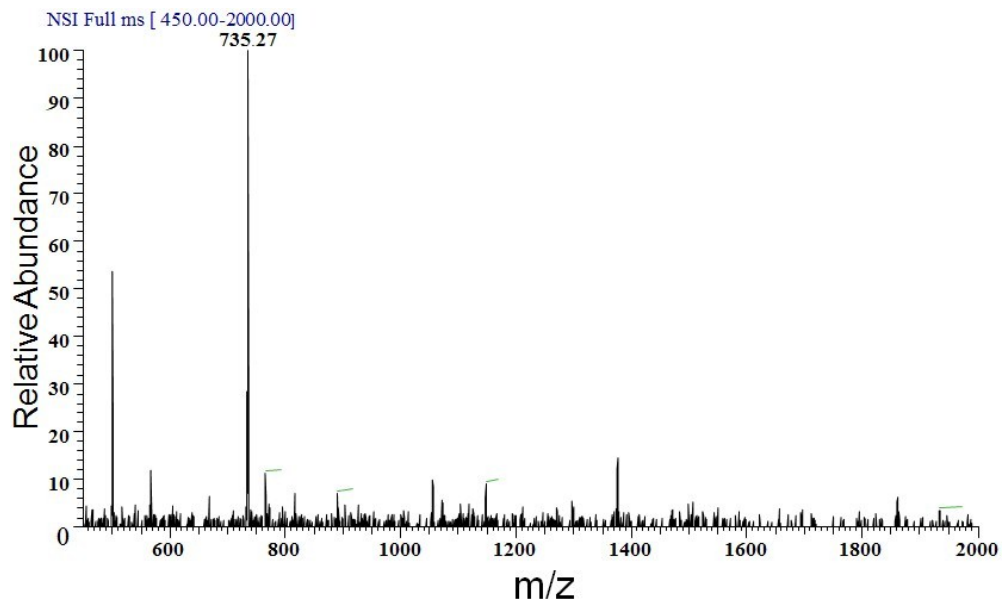


Figure S3 ESI-MS spectrum for **2·H₂O** in MeCN.

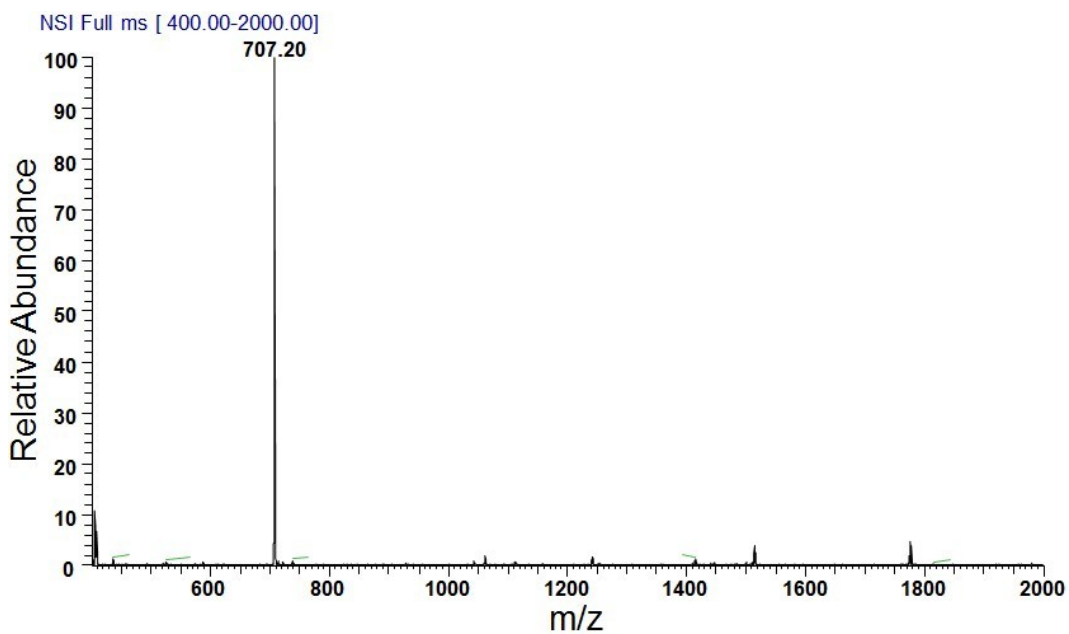


Figure S4 ESI-MS spectrum for **3·MeOH** in MeCN.

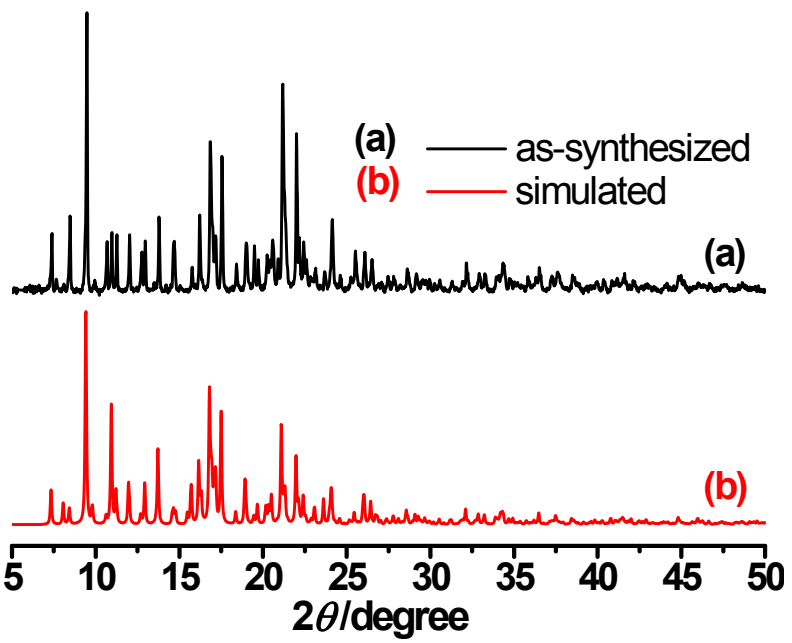


Figure S5 X-ray powder diffraction diagrams of $2 \cdot \text{H}_2\text{O}$ and the simulated spectra from single crystal data.

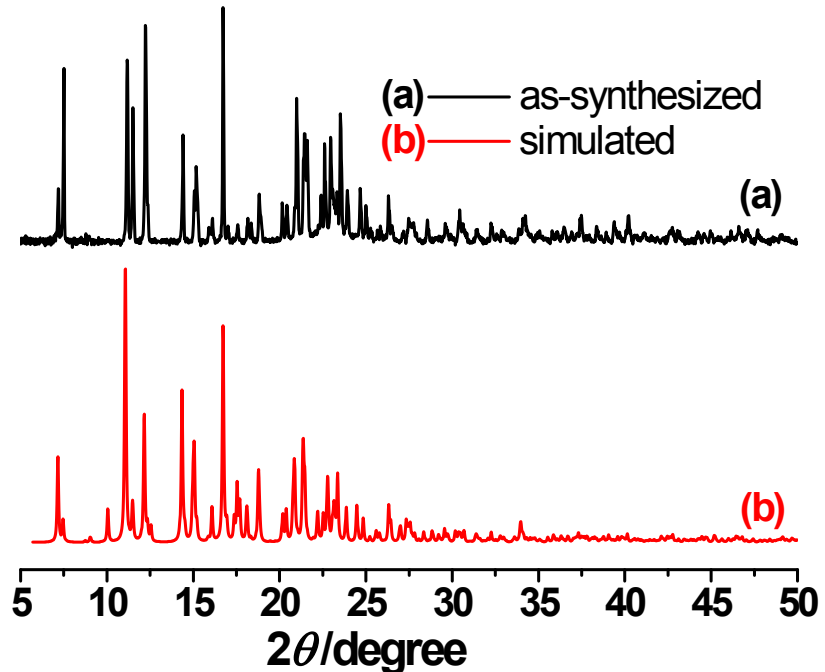


Figure S6 X-ray powder diffraction diagrams of $3 \cdot \text{MeOH}$ and the simulated spectra from single crystal data.

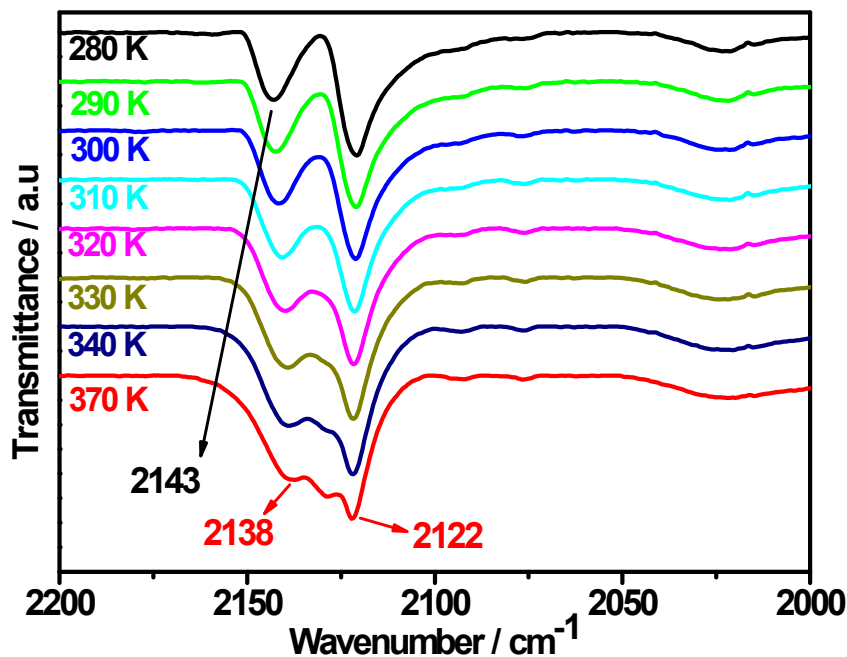


Figure S7 Variable-temperature FT-IR for $2 \cdot \text{H}_2\text{O}$ (Nujol mull, KBr plates), heating from 280 to 370 K.

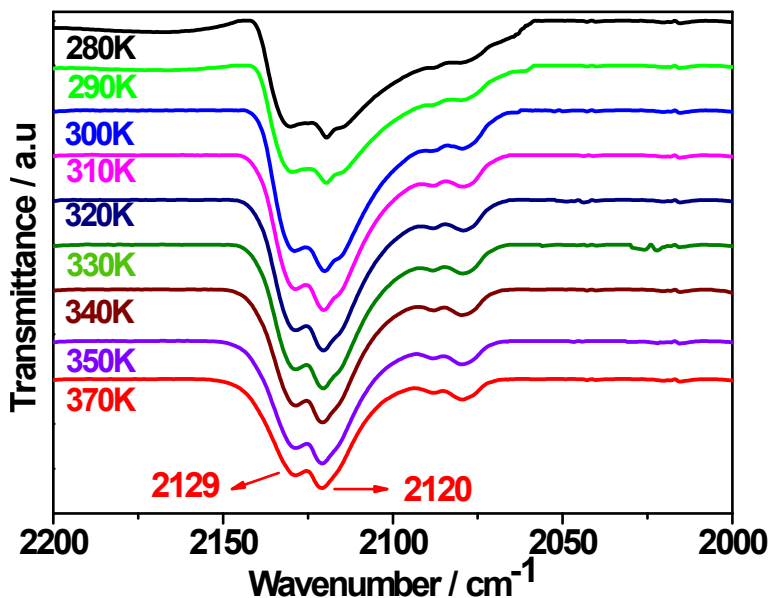


Figure S8 Variable-temperature FT-IR for $3 \cdot \text{MeOH}$ (Nujol mull, KBr plates), heating from 270 to 380 K.

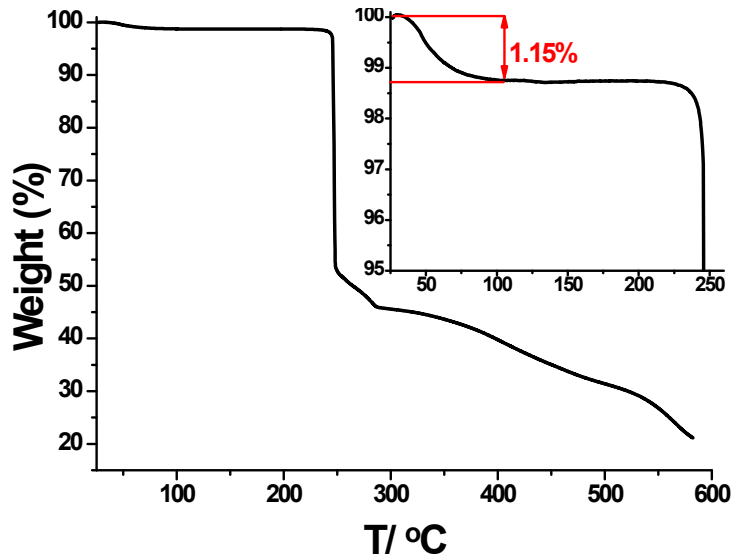


Figure S9 Thermogravimetric analysis of **2**·H₂O. The first weigh loss until 110 °C was due to the coordinated and uncoordinated H₂O molecule (obsd 1.15%, cacl 1.07%). The decomposition of the organic links in the anhydrous compound occurs at 220 °C.

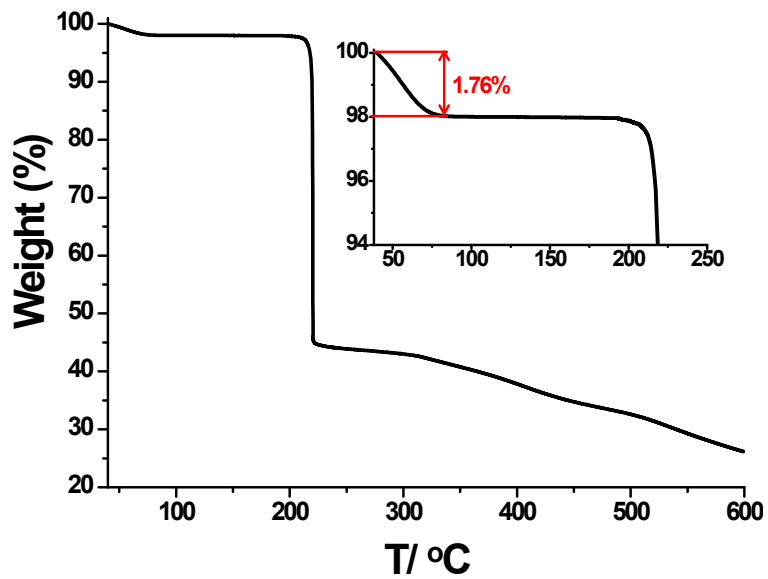


Figure S10 Thermogravimetric analysis of **3**·MeOH. The first weigh loss until 70 °C was due to the coordinated and uncoordinated MeOH molecule (obsd 1.76%, cacl 1.94%). The decomposition of the organic links in the anhydrous compound occurs at 208 °C.

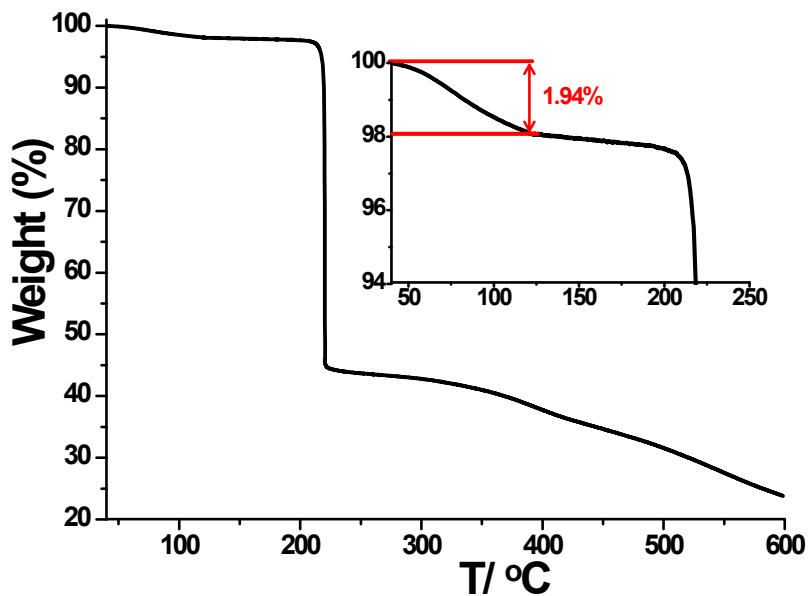


Figure S11 Thermogravimetric analysis of **3·2H₂O**. The first weigh loss until 124 °C was due to the loss of H₂O molecules (obsd 1.94%, cacl 2.21%). The decomposition of the organic links in the anhydrous compound occurs at 210 °C.

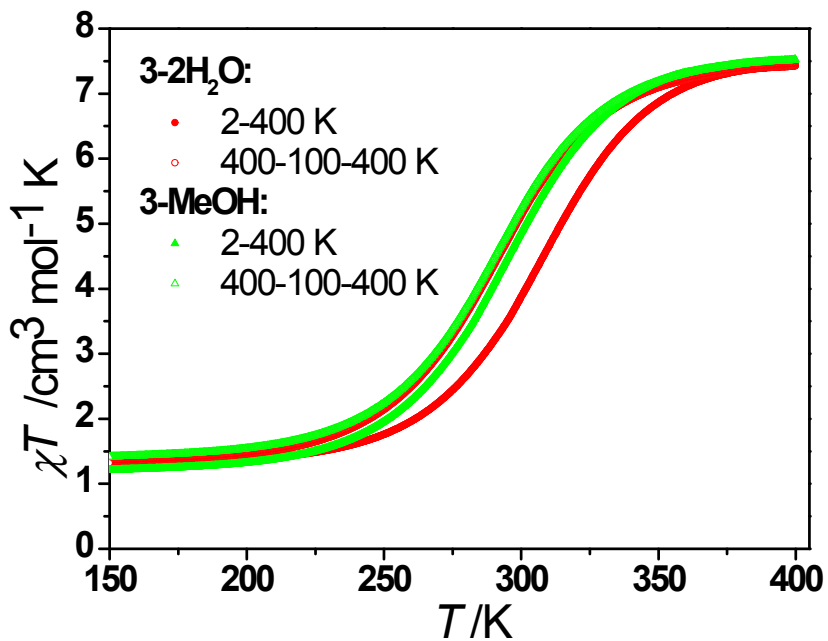


Figure S12 Temperature dependence of $\chi_M T$ plots for **3·MeOH** and **3·2H₂O**.

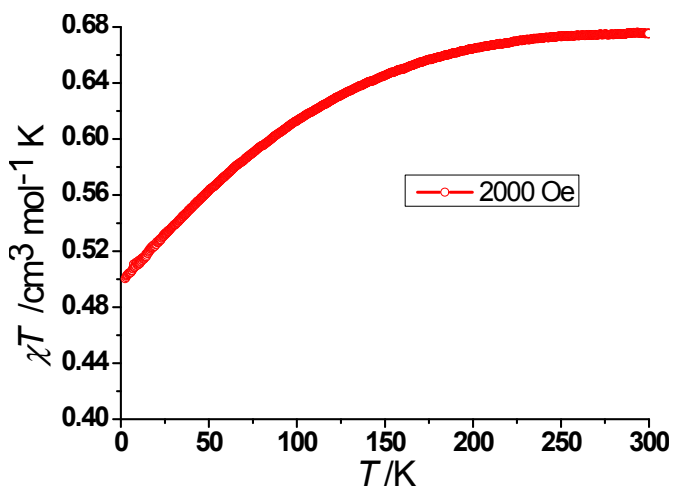


Figure S13 Temperature dependence of $\chi_M T$ plot for **1**.

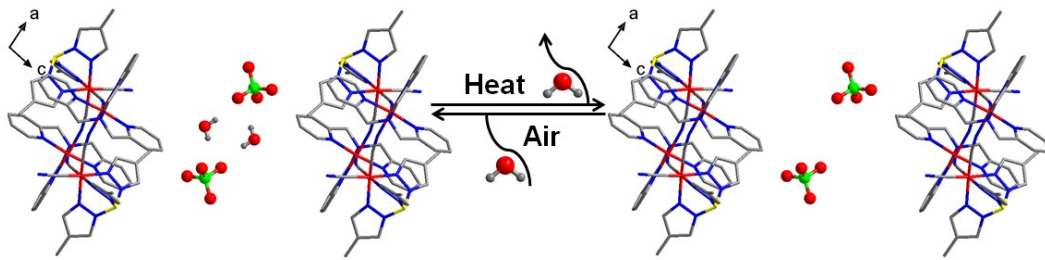


Figure S14 Schematic representation of reversible water desorption and re-sorption between **2·H₂O** and **2**.

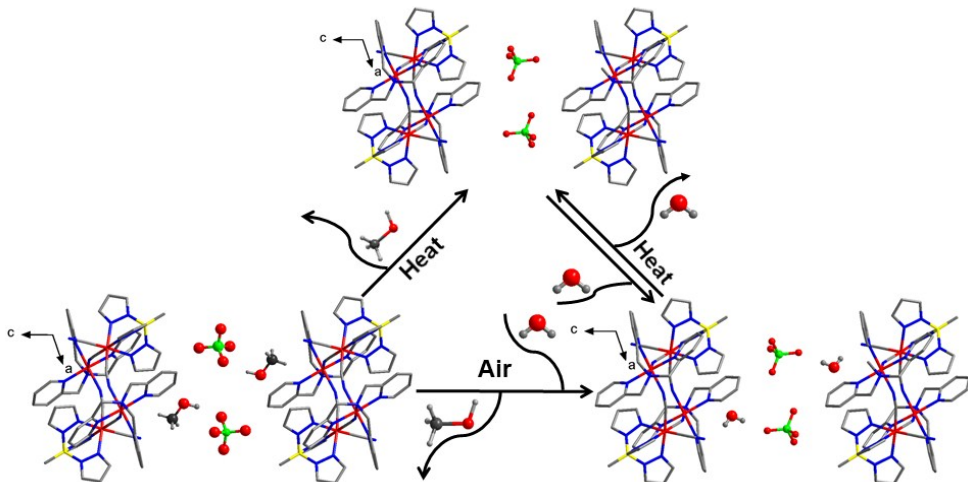


Figure S15 Schematic representation of reversible solvent molecule exchange between **3·MeOH** and **3·2H₂O**.

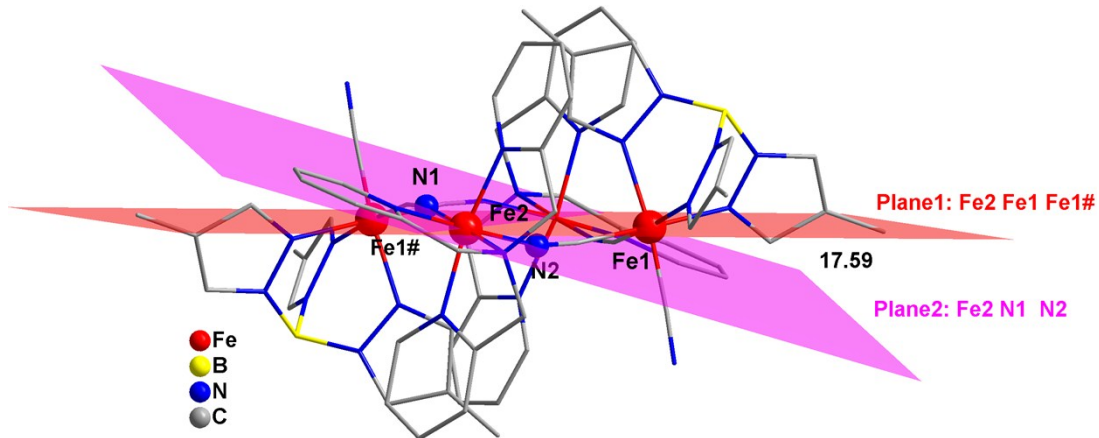


Figure S16 The dihedral angle between the plane1 (Fe2, Fe1, Fe1 $\#$) and the plane2 (Fe2, N1, N2) in **2**. $\# = 1-x, 2-y, -z$

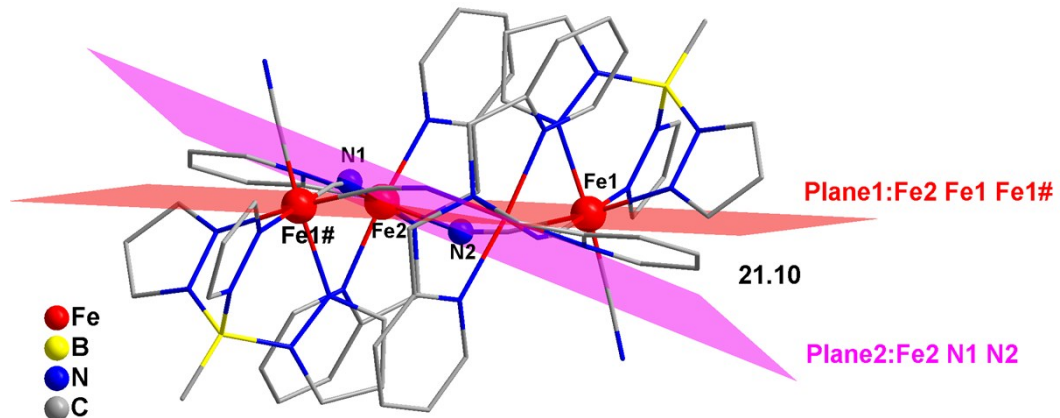


Figure S17 The dihedral angle between the plane1 (Fe2, Fe1, Fe1 $\#$) and the plane2 (Fe2, N1, N2) in **3**. $\# = 1-x, 2-y, 1-z$

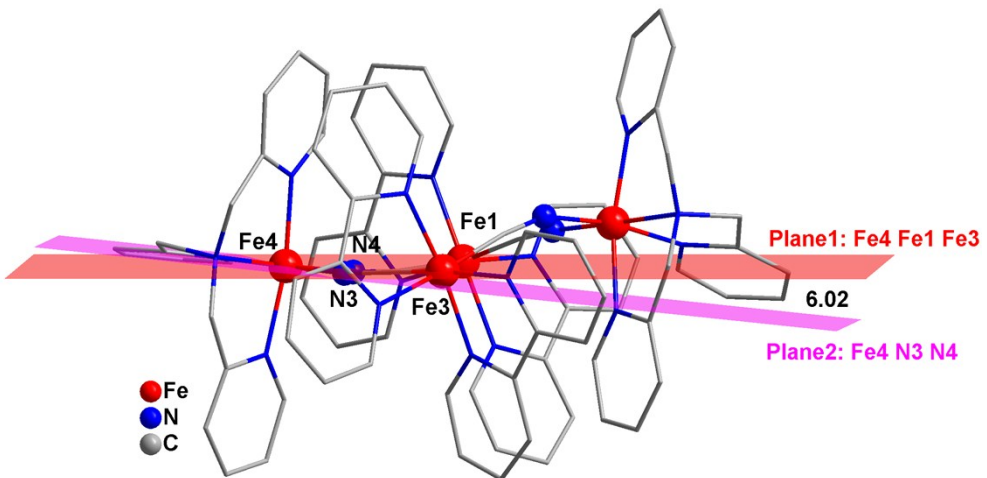
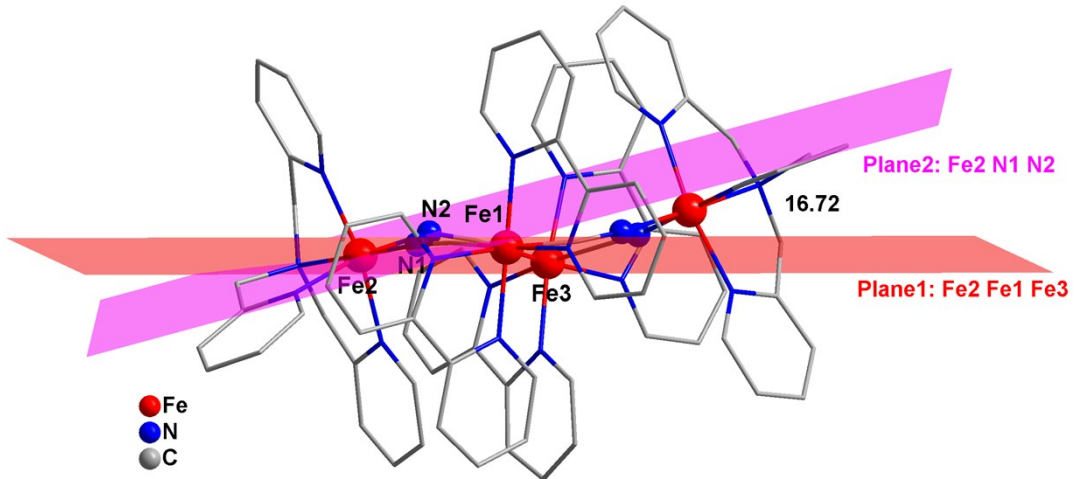


Figure S18 The dihedral angles between (top) the plane1 ($\text{Fe}2, \text{Fe}1, \text{Fe}3$) and the plane2 ($\text{Fe}2, \text{N}1, \text{N}2$), (bottom) the plane1 ($\text{Fe}4, \text{Fe}1, \text{Fe}3$) and the plane2 ($\text{Fe}4, \text{N}3, \text{N}4$) in $[\text{Fe}^{\text{II}}_4(\text{CN})_4(\text{bpy})_4(\text{tpa})_4](\text{PF}_6)_4$. Crystallographic data of $[\text{Fe}^{\text{II}}_4(\text{CN})_4(\text{bpy})_4(\text{tpa})_4](\text{PF}_6)_4$ is obtained from CCDC.

Table S1. Crystal data and structure refinement for **1**.

1	
Formula	C ₃₅ H _{35.5} BFeN _{9.5} P
Formula weight	686.86
Crystal system	Monoclinic
Space group	C2/c
Temperature/K	100
<i>a</i> /Å	40.799(9)
<i>b</i> /Å	8.793(2)
<i>c</i> /Å	23.324(5)
α /°	90
β /°	124.866 (2)
γ /°	90
<i>V</i> /Å ³	6865(3)
Z	8
ρ calcd/g cm ⁻³	1.329
μ / mm ⁻¹	0.526
Collected reflections	26708
Unique reflections	6399
Goodness-of-fit on <i>F</i> ²	1.018
<i>R</i> ₁ [<i>I</i> >2σ (<i>I</i>)]	0.0264
<i>wR</i> ₂ [<i>I</i> >2σ (<i>I</i>)]	0.0697

Table S2. Selected bond lengths [\AA] and angles [$^\circ$] for **1**

1					
Fe1–C1	1.9322(14)	C1–Fe1–C2	88.36(6)	N1–C1–Fe1	177.77(13)
Fe1–C2	1.9224(14)	C1–Fe1–C3	89.49(6)	N2–C2–Fe1	176.57(12)
Fe1–C3	1.9266(14)	C2–Fe1–C3	86.16(6)	N3–C3–Fe1	178.42(13)
Fe1–N4	1.9911(12)	N4–Fe1–N6	87.52(5)		
Fe1–N6	1.9641(12)	N4–Fe1–N8	88.97(5)		
Fe1–N8	1.9772(12)	N6–Fe1–N8	87.63(5)		